

Infrared-Laser-Induced Thermocapillary Deformation and Destabilization of Thin Liquid Films on Moving Substrates

H. M. J. M. Wedershoven, C. W. J. Berendsen, J. C. H. Zeegers, and A. A. Darhuber*

*Department of Applied Physics, Mesoscopic Transport Phenomena Group,
Eindhoven University of Technology, Postbus 513, 5600 Eindhoven, Netherlands*

(Received 2 July 2014; revised manuscript received 14 November 2014; published 19 February 2015; publisher error corrected 27 February 2015)

We study the thermocapillary deformation, induced by infrared laser irradiation, of thin liquid films on moving substrates. We develop numerical models for the temperature distribution and film thickness evolution. Steady-state film thickness profiles are measured for different values of substrate speed and laser power. The experimental results compare well with the simulations. In the case of partially wettable substrates, the thin liquid films tend to become unstable. We find that, for certain ranges of the laser power and substrate speed, the film ruptures in a single location and subsequently dewets without the occurrence of residual droplets. Such “clean” dewetting is highly desirable in the context of immersion lithography or solution processing of organic electronic devices.

DOI: 10.1103/PhysRevApplied.3.024005

I. INTRODUCTION

The interaction of a laser beam with thin liquid films has been studied in the context of many technological applications. In heat-assisted magnetic recording, an ultrathin layer of hard disk lubricant is depleted by evaporation and thermocapillary shear induced by a scanning laser spot [1,2]. Focused laser beams are used for cutting and welding of metals [3,4], deposition of polymer nanoassemblies onto a substrate from solution [5], and curing of inkjet-printed nanoparticle suspensions [6]. Thermocapillary flow is utilized as an actuation mechanism in microfluidic devices [7–24], for the visualization of infrared intensity distributions [25–27], accelerated spreading [28–30], and laser-induced pattern generation in ultrathin metal films [31–37]. Vieyra *et al.* use spatially modulated infrared irradiation for the solution processing of organic electronic devices [38].

The deformation of liquid films due to nonuniform temperature distributions has been investigated extensively [39–56]. The destabilization, *i.e.*, rupture, of thin liquid films by means of temperature gradients has been studied in the case of free films [57–61], *i.e.*, films maintaining two liquid-air interfaces such as soap lamellae. The rupture of films supported by a solid substrate [62–70] is highly relevant to film cooling. Singer *et al.* employ a 532-nm laser to induce dewetting in polystyrene films [71].

In immersion lithography [72,73], a layer of water is enclosed between the objective lens and a wafer covered with photoresist, in order to increase the optical resolution. Above a critical scanning speed, a thin film of water is entrained on the wafer. This film is unstable and breaks up

into droplets. The motivation for this study is to investigate the suitability of an infrared laser beam to speed up and control the rupture process.

In this paper, we present a systematic study of the thermocapillary deformation and rupture of a nonvolatile thin liquid film due to temperature gradients induced by an infrared laser beam. In Sec. II, we describe the experimental setup. Section III introduces the numerical models used for heat transfer and the redistribution dynamics of the thin liquid film. In Sec. IV A, we present a quantitative comparison of numerical and experimental results for the deformation of completely wetting films. Section IV B focuses on the rupture process on partially wetting substrates. We find that rupture can occur without the appearance of residual droplets, which is beneficial to technological applications. We vary the substrate speed and laser power to identify and characterize the corresponding process window.

II. EXPERIMENTS

Figure 1(a) shows a schematic representation of the experimental setup. A thin liquid film of initial thickness h_0 is deposited on the top side of a polycarbonate substrate by spin coating. The resulting initial film thickness is measured with a spectral-interference technique [74]. The substrate is then rotated with a constant angular velocity Ω while being illuminated by a focused infrared (IR) laser beam. The substrate is transparent to visible light but partially absorbs the IR light. The laser beam induces a nonuniform temperature distribution, which causes thermocapillary flow of the thin film. The subsequent deformation and possible rupture of the thin film is monitored *in situ* by using dual-wavelength interference microscopy [75]. The imaging optics is protected from IR light by a short-pass filter (Schott, KG-1), and, in order to avoid

*Corresponding author.
a.a.darhuber@tue.nl

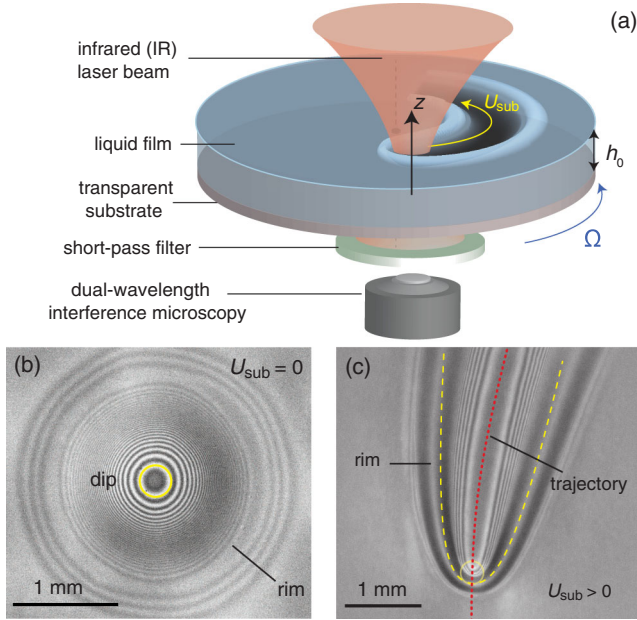


FIG. 1. (a) Schematic representation of the experimental setup for the deformation of a thin liquid film on a moving substrate by a focused infrared laser (dimensions not to scale). (b) Deformation of a thin squalane film on a stationary PC substrate with $h_0 = 5.5 \mu\text{m}$ and $P = 0.3 \text{ W}$. The image is taken 5 s after the laser is switched on. (c) Interference micrograph of the steady-state deformation of a thin film of squalane on a moving PC substrate. The initial film thickness is $h_0 = 4.5 \mu\text{m}$, the laser power $P = 7.8 \text{ W}$, and the substrate speed $U_{\text{sub}} = 5 \text{ mm/s}$.

undesired reflections of visible light from the laser optics, we install a long-pass filter (Edmund Optics, product number 43-949) between the laser focusing optics and the focal plane.

Figure 1(b) shows the deformation of the liquid film in the case of a stationary substrate ($\Omega = 0$). The yellow circle indicates the size and position of the laser spot. In this case, a local depression (“dip”) is formed in the liquid film at the location of the laser spot. This dip is surrounded by a rim. Figure 1(c) illustrates the formation of a track in the liquid film along the laser trajectory in the case of a moving substrate. The liquid that is displaced from the track center line accumulates in a rim upstream of the laser spot and flanking the track center line. The yellow circle indicates the size and position of the laser spot, and the dotted red line its trajectory. The width of the track increases with increasing distance from the laser spot.

The material properties of the substrate material polycarbonate (PC), the wetting liquid squalane, and the partially wetting liquid tri(ethylene glycol) (3EG) are provided as Supplemental Material [76].

A. Infrared laser illumination

The light source is a multimode diode laser system (Lumics LU1470C20-C with an OsTech LSx1 laser diode

driver) with a center wavelength of $\lambda = 1470 \text{ nm}$ and a maximum output power of 20 W. The diverging laser light exiting from the fiber output (diameter $400 \mu\text{m}$, numerical aperture $\text{NA} = 0.22$) is refocused to a spot in the order of $200 \mu\text{m}$ ($\text{NA} = 0.54$). We adjust the laser power range by controlling the current to the laser diode. Linear variation of laser power P within the selected power range is achieved by modulating the laser at a frequency of 50 Hz and using a variable duty cycle.

We characterize the intensity profile $I(r, z)$ of the laser beam by using a home-built scanning slit setup. The propagation direction of the laser beam coincides with the z axis [as indicated in Fig. 1(a)], while r is the radial distance from the optical axis of the beam. We install a solid metal plate with a $25\text{-}\mu\text{m}$ -wide slit in front of the active area of a laser power meter (Thorlabs, S314C/PM100USB) and place the assembly on a motorized translation stage (Newport, UTS100CC). Control and readout of the translation stage and sensor is done by using LABVIEW software (National Instruments). Because of the long time constant of the thermal power meter, the scan speed is very small ($10 \mu\text{m/s}$) to obtain optimal resolution. The measurement is done at low laser power (approximately 0.8 W) to prevent damage to the slit. For a Gaussian beam profile and a sufficiently small ratio of slit width and beam width, the measured profile has the same shape as the beam profile [77].

The resulting profiles are shown in Fig. 2(a). Figure 2(b) shows the intensity distribution obtained from a ray-tracing simulation (Radiant Zemax) of the focusing optics used in the experiments. The dotted lines represent radial intensity profiles at different values of z . Because of aberrations of the optical components as well as small alignment errors, the beam profile is non-Gaussian. Above the focal plane (for positive values of z), the maximum intensity of the beam is located off center. In the focal plane, the beam profile exhibits a narrow peak with a slightly widened base.

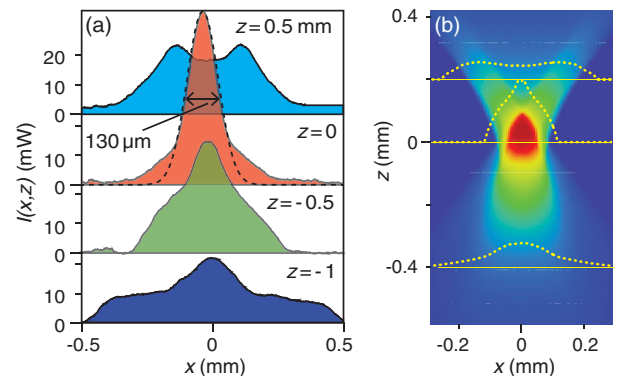


FIG. 2. Intensity profiles $I(x, z)$ of the laser beam. (a) Experimental profiles from the scanning slit measurement. The dashed line represents the numerical approximation of Eq. (1) at $z = 0$. (b) Intensity distribution derived from a ray-tracing simulation of the focusing optics used in the experiments. The dotted lines represent intensity profiles at different heights z .

The full width at half maximum (FWHM) is approximately $130 \mu\text{m}$. Below the focal plane (i.e., for negative values of z), the peak intensity decreases and the beam width increases. In our experiments, we position the top surface of the substrate into the focal plane of the optical setup ($z = 0$). The vertical alignment is performed with the help of an Omega CHAL-001 thermocouple with a head diameter of approximately $25 \mu\text{m}$, resulting in a position uncertainty of approximately $50 \mu\text{m}$.

III. NUMERICAL MODELS

In order to simulate the thermocapillary deformation of a thin liquid film on a substrate that is moving relative to a laser beam, we couple a model for the temperature distribution with a second model for the thin-film redistribution. We assume that the material properties of the liquid (surface tension, viscosity, and density—see Supplemental Material [76]) depend on the local temperature $T(x, y, z, t)$. We use Cartesian coordinates (x, y, z) and assume that the substrate moves with a constant velocity U_{sub} in the positive y direction. This is a good approximation provided that the distance between the optical axis and the axis of rotation of the substrate is sufficiently large. In the experiments, this distance is approximately 15 mm .

We approximate the nonuniform beam profiles shown in Fig. 2 by a Gaussian distribution of variable width $w(z)$:

$$I = \frac{2P}{\pi[w(z)]^2} \exp\left(-2\frac{x^2 + y^2}{[w(z)]^2}\right) \exp(-\alpha_{\text{PC}}|z|). \quad (1)$$

The line $x = y = 0$ corresponds to the optical axis of the laser beam, and the plane $z = 0$ corresponds to its focal plane. The last term of Eq. (1) ensures that the intensity decays exponentially in the negative z direction. The value of the absorption coefficient α_{PC} of the PC substrate for the IR irradiation is given in Supplemental Material [76]. The prefactor of Eq. (1) ensures that the xy -integrated intensity is equal to $P \exp(-\alpha_{\text{PC}}|z|)$. The dashed line in Fig. 2(a) corresponds to a fit to the experimental intensity profile $I(r, z = 0)$, from which we determine $w_0 = 120 \mu\text{m}$. The beam width $w(z)$ is assumed to increase linearly according to $w(z) = w_0 + a|z|$. From the data shown in Fig. 2(a), we determine $a = 0.3$.

The nonuniform laser heating results in temperature gradients at the liquid-air interface. The corresponding thermocapillary shear stress drives the flow of liquid away from the heated region [13]. Since the initial thickness of the thin film h_0 is much smaller than w_0 , we use the lubrication approximation [78] to model the evolution of the film thickness $h(x, y, t)$.

The details of the two models (equations, boundary conditions, and numerical aspects) are described in Appendixes A and C. Appendixes B and D characterize the resulting time-dependent temperature distribution and

thin-liquid-film deformation. In the remainder of this section, we will focus on the effect of the substrate speed on the steady-state temperature distribution.

A. Effect of substrate speed U_{sub} on temperature distribution

Figures 3(a)–3(c) show steady-state surface temperature profiles $\Delta T_s(x, y) \equiv T(x, y, z = 0) - T_0$ for substrate speeds U_{sub} of 2, 8, and 32 mm/s, respectively. The uniform initial temperature T_0 is 293 K. The profiles are normalized with $\max[\Delta T_s]$, the corresponding maximum temperature rise. Heat is convected in the y direction due to the motion of the substrate and spreads via conduction in the x direction. Therefore, the surface temperature profile widens with increasing distance from the laser spot. The solid black lines in Figs. 3(a)–3(c) connect the points where $\Delta T_s(x, y) = \frac{1}{2} \Delta T_s(x = 0, y)$. They thus indicate the FWHM of the temperature distribution. The dotted white line in Fig. 3(a) is a power-law function of the form $\text{FWHM} \sim y^{1/2}$. The width of the temperature distribution decreases for larger values of the substrate speed.

The Peclet number

$$\text{Pe}_w \equiv \frac{U_{\text{sub}} w_0}{k_{\text{sub}} / (\rho_{\text{sub}} c_p)} \quad (2)$$

quantifies the relative importance of convective and diffusive heat transfer. The values of the thermal conductivity k_{sub} , the mass density ρ_{sub} , and the specific heat capacity c_p of the PC substrate are given in Supplemental Material [76].

Figure 4(a) shows the steady-state surface temperature along the track center line $\Delta T_s(x = 0, y, t \rightarrow \infty)$ for different values of U_{sub} . The dotted black line is a power-law function of the form $\Delta T_s \sim y^{-1/2}$. Figure 4(b) shows the

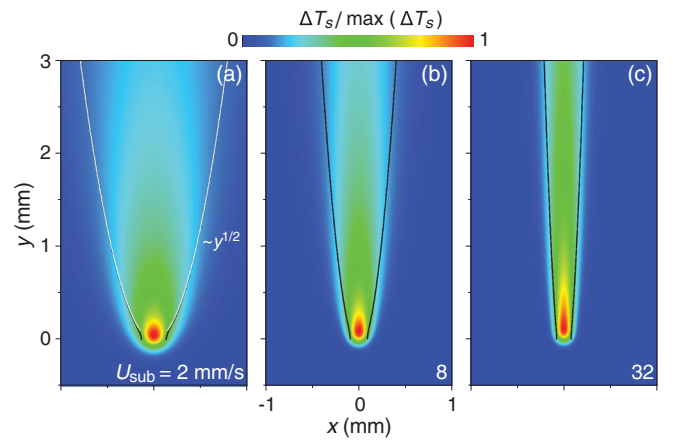


FIG. 3. Simulations of the steady-state surface temperature profile $\Delta T_s(x, y)$ for $P = 8 \text{ W}$ and (a) $U_{\text{sub}} = 2$, (b) 8, and (c) 32 mm/s. The profiles are normalized with the corresponding $\max[\Delta T_s]$. The solid black lines represent the full width at half maximum of the profile. The dotted white line in (a) is a power-law function with an exponent $1/2$.

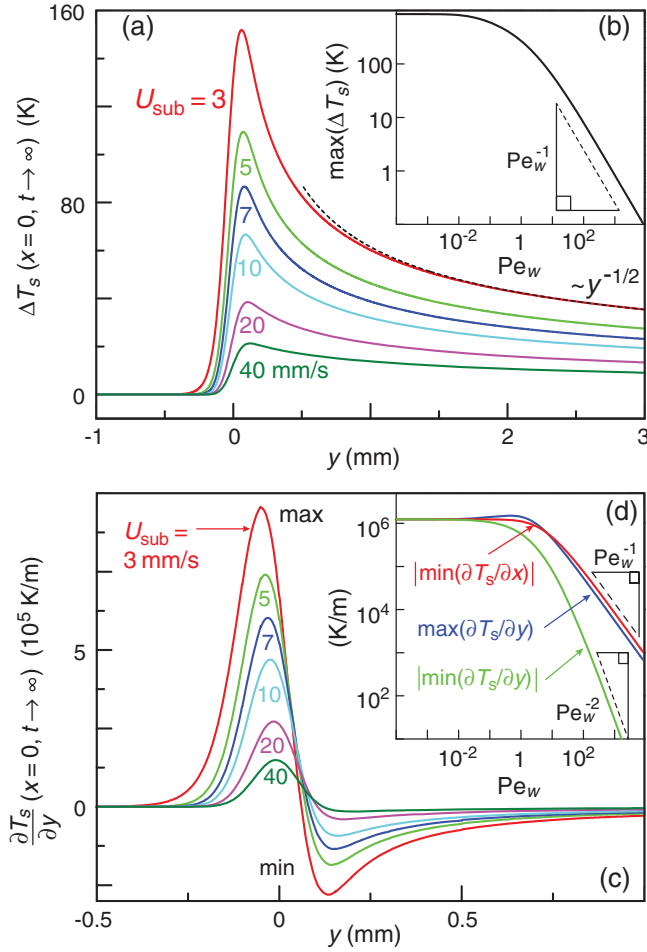


FIG. 4. Numerical results of the heat-transfer model. (a) Steady-state surface temperature rise along the track center line $\Delta T_s(x=0, y)$ for different values of U_{sub} . (b) Maximum temperature rise in steady-state $\max[\Delta T_s]$ as a function of Pe_w . (c) Steady-state surface temperature gradient along the track center line, $\partial T_s/\partial y(x=0, y)$ for different values of U_{sub} . (d) Maximum and minimum absolute values of the y derivative and minimum absolute value of the x derivative in the steady state ($\max[\partial T_s/\partial y]$, $|\min[\partial T_s/\partial y]|$, and $|\min[\partial T_s/\partial x]|$, respectively) as a function of Pe_w .

maximum temperature rise in steady-state $\max[\Delta T_s(t \rightarrow \infty)]$ as a function of Pe_w (w_0 is fixed at $120 \mu\text{m}$). When $Pe_w \ll 1$, the maximum temperature rise is independent of the substrate speed, because in this regime heat conduction dominates over heat convection. When $Pe_w \gg 1$, the temperature rise scales as $\max[\Delta T_s] \sim Pe_w^{-1}$, as indicated by the dashed line in Fig. 4(b) [79]. In this regime, heat convection dominates over heat conduction. Typical values for our experiments are $1 < Pe_w < 8$.

Figure 4(c) shows the steady-state y derivative of the temperature along the center line, $\partial T_s/\partial y(x=0)$ for different values of U_{sub} . Both its maximum value $\max[\partial T_s/\partial y]$ and its minimum absolute value $|\min[\partial T_s/\partial y]|$ decrease for increasing values of U_{sub} .

This is shown more systematically in Fig. 4(d), where additionally the minimum absolute value of the x derivative $|\min[\partial T_s/\partial x]|$ is plotted as a function of Pe_w . In the conduction-dominated regime ($Pe_w \ll 1$), $\max[\partial T_s/\partial y] = |\min[\partial T_s/\partial y]| = |\min[\partial T_s/\partial x]|$, and all three derivatives are independent of U_{sub} . In the convection-dominated regime ($Pe_w \gg 1$), both $\max[\partial T_s/\partial y]$ and $|\min[\partial T_s/\partial x]|$ scale as Pe_w^{-1} , while $|\min[\partial T_s/\partial y]|$ scales as Pe_w^{-2} . The derivation of these scaling relations is discussed in Appendix A.

IV. RESULTS AND DISCUSSION

A. Completely wetting films

Figure 5 shows the steady-state deformation of a thin squalane film on a moving substrate for a laser power of $P = 8 \text{ W}$. Figures 5(a)–5(c) are obtained from numerical simulations with substrate speeds of 2, 8, and 32 mm/s, respectively. These values of U_{sub} correspond to those used in Fig. 3. The profiles are normalized with the maximum film thickness h_{max} that occurs off center in the rim. This normalization is the reason why the undisturbed film thickness $h_0 = 5 \mu\text{m}$ is represented by different colors in Figs. 5(a)–5(c).

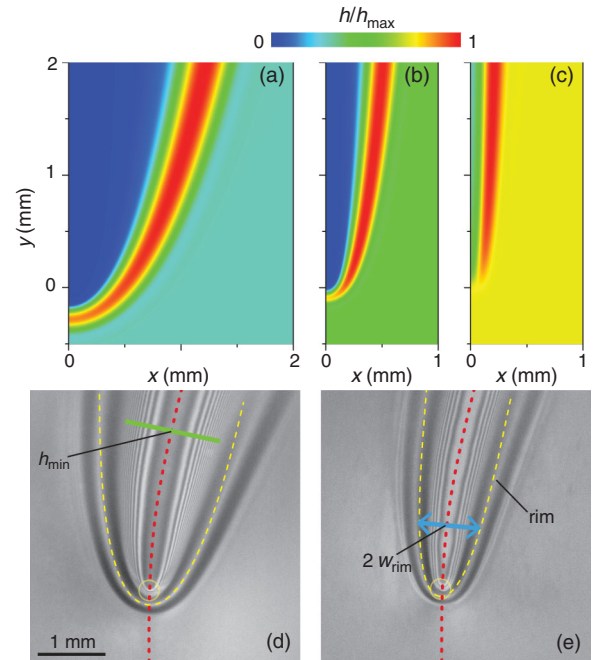


FIG. 5. (a)–(c) Simulations of the steady-state thin-liquid-film profile $h(x, y)$ for $P = 8 \text{ W}$ and (a) $U_{\text{sub}} = 2$, (b) 8, and (c) 32 mm/s. The profiles are normalized with the corresponding maximum film thickness (a) $h_{\text{max}} = 17$, (b) 12, and (c) $7 \mu\text{m}$. (d), (e) Experimental interference micrographs of the steady-state deformation of a thin film of squalane on a moving PC substrate with $P = 7.8 \text{ W}$ and (d) $U_{\text{sub}} = 3$ and (e) 7 mm/s. The yellow circles indicate the size and position of the laser beam, and the dotted red line its trajectory.

The liquid in front of the laser spot is displaced by the thermocapillary stresses and accumulates into a rim flanking the track center line. The track width increases with increasing value of y , which reflects the widening of the temperature profiles shown in Fig. 3. The track width decreases with increasing value of U_{sub} , because the temperature profile narrows as shown in Fig. 3. The thickness of the rim upstream of the track is lower than that of the rim flanking the track.

Figures 5(d) and 5(e) show interference micrographs of the steady-state deformation for $U_{\text{sub}} = 3$ and 7 mm/s, respectively. The measurement for $U_{\text{sub}} = 5$ mm/s is shown in Fig. 1(c). The dashed yellow lines in Figs. 1(c), 5(d), and 5(e) indicate the rim shapes as obtained from the numerical simulations, which agree well with the experimental shapes, especially in the vicinity of the laser spot. For positions further away from the laser spot, the experimental rim shapes deviate slightly, because in the numerical model we assume that the substrate moves in a straight line, whereas in our experimental setup the substrate is rotating.

The minimum film thickness of the profile, h_{min} , occurs along the laser trajectory, as indicated in Fig. 5(d). Using dual-wavelength interference microscopy [75], we are able to determine the absolute film thickness profile along a cross section as indicated with the green line segment in Fig. 5(d). We determine h_{min} at six different positions along the laser trajectory. The values of h_{min} that are reported in the remainder of this manuscript are the average of these values. For the corresponding error bars, we take the standard deviation of these six values.

Figure 6(b) shows simulations of the steady-state center line film profile $h(x=0)$ for different values of U_{sub} for $P = 8$ W and $h_0 = 5$ μm . For increasing U_{sub} , the height

of the rim decreases, the position of the maximum shifts to increasing (i.e., less negative) values of y , and the minimum film thickness increases. This is shown more quantitatively in Fig. 6(a), where h_{min} is plotted as a function of U_{sub} . The red circles are obtained from experiments, and the solid red line is a power-law fit $h_{\text{min}} \sim U_{\text{sub}}^\beta$ with exponent $\beta = 2.3$. The green squares and blue diamonds correspond to numerical simulations for beam radii of $w_0 = 120$ and 150 μm , respectively. The simulations reproduce the power-law exponent $\beta = 2.3$ of the experiments very well. A reason the simulations for $w_0 = 150$ μm provide a better agreement could be that the laser beam may have been slightly out of focus during the experiments.

Figure 7(b) shows simulations of the steady-state center line height profile $h(x=0)$ for different values of P . The substrate speed U_{sub} is 3 mm/s, and the initial film thickness $h_0 = 5$ μm . For increasing laser power, the height of the rim increases and the minimum film thickness decreases. In Fig. 7(a), h_{min} is plotted as a function of P . The red circles and cyan and magenta triangles represent experimental data. For the red circles, the frequency of the duty cycle signal for the laser modulation is 50 Hz. A power-law fit of the form $h_{\text{min}} \sim P^{-\alpha}$ gives an exponent $\alpha = 1.8$. For the cyan triangles, the frequency of the duty cycle signal is increased to 5000 Hz, and for the magenta triangles, the laser is not modulated. The exponent of the power-law fit in both cases is equal to $\alpha = 2.0$. The green squares and blue diamonds are obtained from numerical simulations with $w_0 = 120$ and 150 μm , respectively. The power-law exponent α for the numerical data is equal to 2.2, i.e., slightly larger than for the experiments.

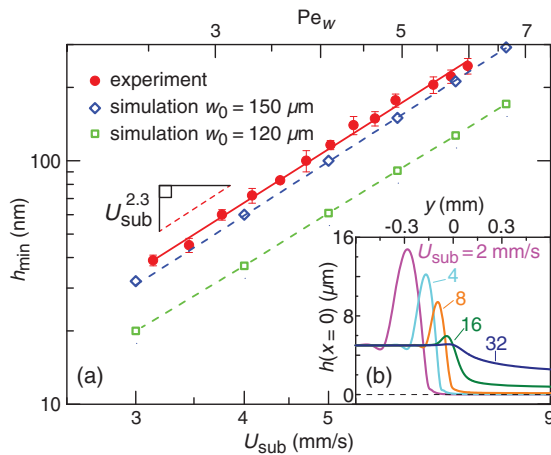


FIG. 6. (a) Minimum film thickness h_{min} as a function of the substrate speed U_{sub} . The red circles are obtained from experiments ($P = 7.8$ W and $h_0 = 4.5$ μm) and the blue diamonds and green squares from numerical simulations ($P = 8$ W, $h_0 = 5.0$ μm , and $w_0 = 120$ or 150 μm). (b) Numerical simulations of the steady-state centerline film profile $h(x=0)$ for different values of U_{sub} .

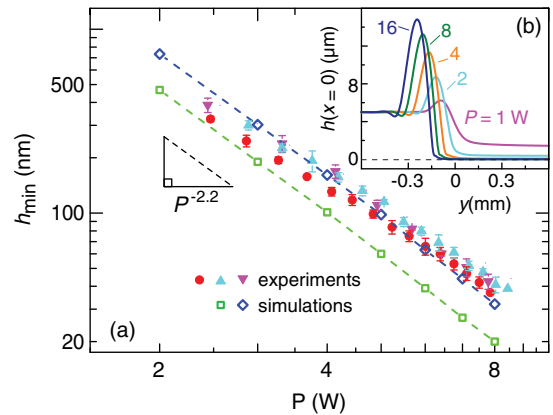


FIG. 7. (a) Minimum film thickness h_{min} as a function of laser power P . The red circles and the cyan and magenta triangles are obtained from experiments ($U_{\text{sub}} = 3.1$ mm/s, $h_0 = 4.5$ μm), with a duty cycle frequency of 50 Hz (red), 5000 Hz (cyan), or no duty cycle (magenta). The blue diamonds and green squares are obtained from numerical simulations ($U_{\text{sub}} = 3$ mm/s, $h_0 = 5.0$ μm , and $w_0 = 120$ or 150 μm). (b) Numerical simulations of the steady-state center line film profile $h(x=0)$ for different values of P .

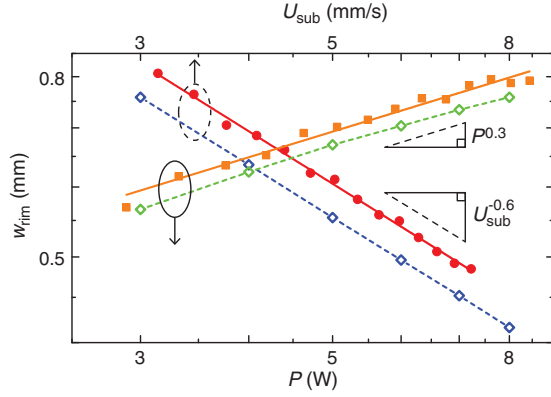


FIG. 8. Rim width w_{rim} as a function of laser power P (bottom axis) and substrate speed U_{sub} (top axis). The orange squares are obtained from experiments (with $U_{\text{sub}} = 3.1$ mm/s, $h_0 = 4.5$ μm , and a duty cycle frequency of 5000 Hz) and the green diamonds from numerical simulations ($U_{\text{sub}} = 3$ mm/s, $h_0 = 5.0$ μm , and $w_0 = 150$ μm). The red circles represent experimental data ($P = 7.8$ W, $h_0 = 4.5$ μm , and a duty cycle frequency of 50 Hz) and the blue diamonds numerical simulations ($P = 8$ W, $h_0 = 5.0$ μm , and $w_0 = 150$ μm).

We determine the width of the rim at a distance of $8w_0$ from the position of the laser beam. This width is called w_{rim} and is indicated in Fig. 5(e) with a blue arrow. Figure 8 shows w_{rim} as a function of P and U_{sub} in a double-logarithmic plot. The red circles and orange squares represent experimental data, and the blue and green diamonds are obtained from numerical simulations. The solid orange and red lines are power-law fits of the form $w_{\text{rim}} \sim P^{c_1}$ and $w_{\text{rim}} \sim U_{\text{sub}}^{-c_2}$, with exponents $c_1 = 0.3$ and $c_2 = 0.6$. The numerical simulations reproduce the exponents very well.

Compared to film deformation by a gas jet [75], h_{min} and w_{rim} now depend more sensitively on the substrate speed U_{sub} . The difference is caused by the driving mechanism of the film deformation, i.e., the temperature gradient, depending strongly on U_{sub} . Moreover, the liquid viscosity is temperature dependent and thus also depends on U_{sub} .

1. Scaling analysis

In the case of a stationary substrate, the minimum thickness h_{min} scales as [70]

$$h_{\text{min}}(t) \sim \frac{2\mu t^{-1}}{\frac{\partial\gamma}{\partial T} \min \left[\frac{\partial^2 T}{\partial x^2} + \frac{\partial^2 T}{\partial y^2} \right]}, \quad (3)$$

where $\partial\gamma/\partial T$ is the temperature coefficient of the surface tension and μ the viscosity. By replacing the time variable t with w_0/U_{sub} , it follows that h_{min} in the case of a moving substrate scales as

$$h_{\text{min}} \sim \frac{2\mu U_{\text{sub}}}{w_0 \frac{\partial\gamma}{\partial T} \min \left[\frac{\partial^2 T}{\partial x^2} + \frac{\partial^2 T}{\partial y^2} \right]}. \quad (4)$$

When we assume a constant, temperature-independent viscosity in our simulations, we obtain a scaling relation $h_{\text{min}} \sim U_{\text{sub}}^\beta$ with exponent $\beta \approx 1.3$ (data not shown). The term $\min \left[(\partial^2 T/\partial x^2) + (\partial^2 T/\partial y^2) \right]$ decreases with increasing U_{sub} , which increases β from a value of 1 to 1.3. According to Eq. (4), the minimum film thickness should scale as $h_{\text{min}} \sim P^{-\alpha}$, where $\alpha = 1$, since the term $\min \left[(\partial^2 T/\partial x^2) + (\partial^2 T/\partial y^2) \right]$ scales linearly with P . This result is reproduced by the simulations using a constant, temperature-independent viscosity, which results in an exponent $\alpha = 1$ (data not shown). Accounting for the temperature dependence of viscosity increases the exponents extracted from simulations to $\beta = 2.3$ and $\alpha = 2.2$, in excellent agreement with the experimental data in Figs. 6(a) and 7(a).

B. Partially wetting films

We study the IR-laser-induced dewetting of partially wetting 3EG films on PC substrates that are moving with respect to the laser beam. Figure 9 shows the deformation of liquid films on moving substrates for different values of U_{sub} . The laser power is $P = 8.2$ W, and the initial film thickness $h_0 = 5$ μm . The yellow circles indicate the position of the laser spot, and the red dashed line its trajectory. For $U_{\text{sub}} = 5.3$ mm/s [Fig. 9(a)], a single dry spot is nucleated in the thin film. This dry spot rapidly dewets the partially wetting substrate, until it reaches the rim of the track. A completely dry track is formed along the trajectory of the laser beam. This dewetting behavior is qualitatively different from the case when a gas jet is used to deform and rupture the thin film [75], where multiple dry spots are nucleated along the track, resulting in a multitude of residual droplets on the substrate. We attribute this different dewetting behavior to a temperature-induced

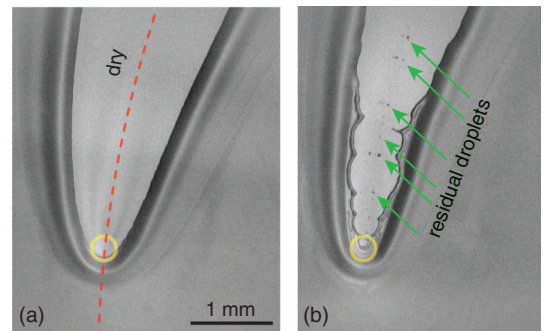


FIG. 9. Interference micrographs of the IR-laser-induced dewetting process of a thin 3EG film on a PC substrate for $P = 8.2$ W, $h_0 = 5$ μm , and substrate speeds U_{sub} of (a) 5.3 and (b) 8.2 mm/s. The yellow circles indicate the position of the laser spot, and the red line its trajectory.

increase in dewetting speed, due to the reduction of the viscosity of the liquid. Figure 9(b) shows that, for $U_{\text{sub}} = 8.2$ mm/s, the track is no longer completely dry and residual droplets are left behind on the substrate (indicated by the green arrows). The most likely reason is that, for an increasing substrate speed, the temperature rise of the substrate decreases [as illustrated in Fig. 4(a)], which increases the rupture time and decreases the dewetting speed. When U_{sub} exceeds the dewetting speed, multiple dry spots are nucleated, and droplets will be deposited on the substrate. We refer to the maximum value of U_{sub} that still results in a dry track as U_{max} . Figure 10 shows U_{max} as a function of the laser power P . The red open circles are obtained from experiments. We estimate the uncertainty in the value of U_{max} to be 0.5 mm/s. The solid red line corresponds to a power-law fit of the form $U_{\text{max}} \sim P^{0.9}$.

In order to rationalize the experimental data, we perform one-dimensional (1D) model calculations, where the laser-induced temperature distribution and the liquid height profile are assumed to be functions of y only. Instead of Eq. (1), we use the 1D intensity distribution

$$I = \frac{\sqrt{2}P_{1D}}{\sqrt{\pi}wc} \exp\left(-2\frac{y^2}{w^2}\right), \quad (5)$$

where the parameter $c = 150 \mu\text{m}$ has been chosen such that the maximum intensity of Eq. (5) coincides with that of Eq. (1). The parameter P_{1D}/c quantifies the laser power per unit length in the x direction.

For the simulations of partially wetting liquids, we explicitly consider the material-specific interactions

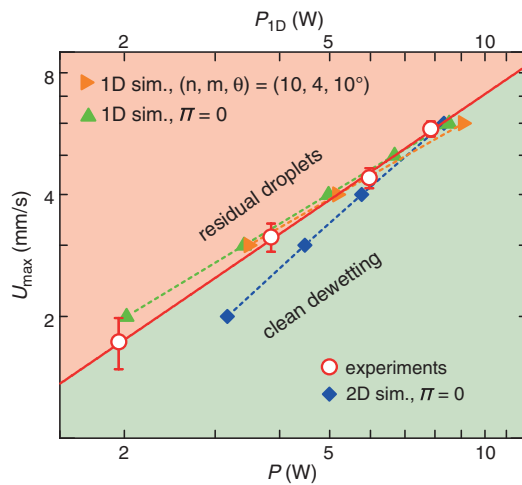


FIG. 10. Double-logarithmic plot of the maximum substrate speed U_{max} as a function of laser power. Red open circles represent experimental data, blue diamonds 2D model calculations without disjoining pressure, green triangles 1D model calculations without disjoining pressure, and orange triangles 1D model calculations including disjoining pressure with parameters $(n, m, h^*, \theta) = (10, 4, 10 \text{ nm}, 10^\circ)$.

between the liquid and the substrate by means of a phenomenological model for the disjoining pressure [80]:

$$\Pi(h) = \gamma(1 - \cos \theta) \frac{(n-1)(m-1)}{(n-m)h^*} \left[\left(\frac{h^*}{h}\right)^n - \left(\frac{h^*}{h}\right)^m \right], \quad (6)$$

where n , m , and h^* are parameters that determine the shape of the disjoining pressure function, θ is the contact angle, and γ is the surface tension.

After switching on the laser, a dip in the height profile forms and excess liquid is pooled up in a rim ahead of the laser spot. The morphology is reminiscent of that shown in Figs. 6(b) and 7(b) with the difference that the rim height keeps growing. The quasi-steady-state liquid height profile in the vicinity of the laser spot is illustrated in Fig. 11(a). The blue line corresponds to a simulation with parameters $(n, m, h^*, \theta) = (3, 2, 10 \text{ nm}, 5^\circ)$ in Eq. (6). The film is thinned from an initial thickness of $h_0 = 5 \mu\text{m}$ down to approximately 30 nm and becomes unstable at $y \approx 0.25$ mm, beyond which a series of nanometer-sized

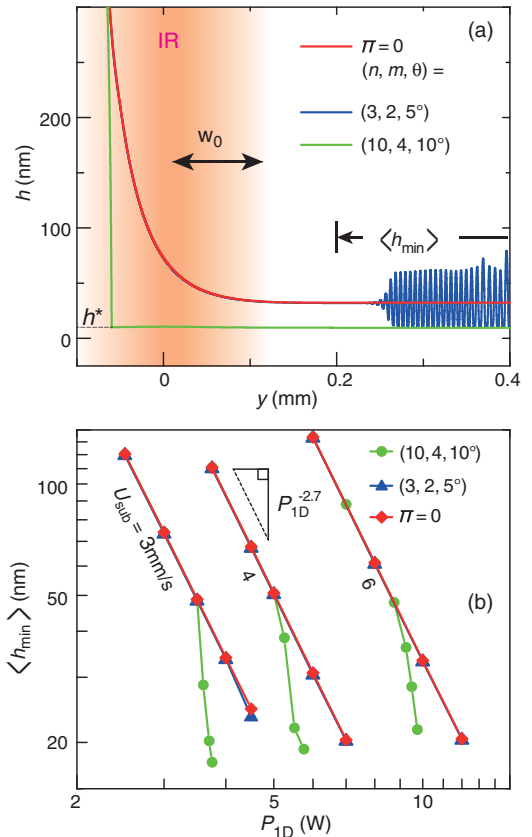


FIG. 11. (a) Height profile in the vicinity of the laser spot for a one-dimensional model and different disjoining pressure parameters for $P_{1D} = 4$ W and $U_{\text{sub}} = 3$ mm/s. The horizontal dotted line indicates the value of h^* . (b) Average minimum film thickness $\langle h_{\text{min}} \rangle$ as a function of P_{1D} for different values of U_{sub} and different disjoining pressure parameters.

droplets is observed. The red curve corresponds to a completely wetting liquid with vanishing disjoining pressure. It essentially coincides with the blue line until $y \approx 0.25$ mm but does not exhibit the instability. The green curve corresponds to disjoining pressure parameters $(n, m, h^*, \theta) = (10, 4, 10 \text{ nm}, 10^\circ)$. In this case, the film thins down to approximately h^* , which in terms of our disjoining pressure isotherm corresponds to an essentially dry surface.

Figure 11(b) shows numerical simulations of the average film thickness $\langle h_{\min} \rangle$ downstream of the laser spot as a function of P_{1D} for different values of U_{sub} . For the determination of $\langle h_{\min} \rangle$, we average the film thickness in the interval $2w_0 < y < 6w_0$ at the time the substrate has moved a distance of approximately $8w_0$ after switching on the laser. The green circles correspond to $(n, m, h^*, \theta) = (10, 4, 10 \text{ nm}, 10^\circ)$, whereas the blue triangles represent $(3, 2, 10 \text{ nm}, 5^\circ)$. The red diamonds correspond to a completely wetting liquid with $\Pi = 0$. The insensitivity of $\langle h_{\min} \rangle$ to the value of Π in the film thickness range $\langle h_{\min} \rangle \gtrsim 5h^* = 50$ nm is clearly visible. The dotted line indicates a power-law relation of the form $\langle h_{\min} \rangle \sim P_{\text{1D}}^{-\alpha}$ with an exponent $\alpha = 2.7$, which approximates the numerical data well for $\langle h_{\min} \rangle \gtrsim 5h^* = 50$ nm. The exponent 2.7 is larger than the value of 2.2 found in Fig. 7(a), due to differences in the temperature dependencies of the viscosity for squalane and 3EG. The data for $(10, 4, 10 \text{ nm}, 10^\circ)$ exhibit a sudden drop in $\langle h_{\min} \rangle$ at a certain power value, which we attribute to the much higher absolute value of Π and the steeper gradient $d\Pi/dh$ for $h \lesssim 5h^* = 50$ nm [81].

In order to compare the experimental data with numerical results for U_{max} , we introduce two criteria: (i) For a given value of U_{sub} , we determine the value of P_{1D} that results in a certain residual film thickness $\langle h_{\min} \rangle = h_{\text{crit}}$, by using curves such as those in Fig. 11(b). Alternatively, (ii) for a given value of U_{sub} , we determine the value of P_{1D} corresponding to the sudden drop in $\langle h_{\min} \rangle$, observed for $(10, 4, 10 \text{ nm}, 10^\circ)$ in Fig. 11(b).

The green triangles in Fig. 10 are obtained from 1D model calculations using the first criterion with $h_{\text{crit}} = 5h^* = 50$ nm. For these simulations, we do not include the disjoining pressure owing to the above-mentioned insensitivity of $\langle h_{\min} \rangle$ to the value of Π . The orange triangles are obtained from 1D model calculations, including the disjoining pressure with parameters $(n, m, h^*, \theta) = (10, 4, 10 \text{ nm}, 10^\circ)$ and using the second criterion. The dashed green and orange lines represent power-law relations $U_{\text{max}} \sim P_{\text{1D}}^{0.75}$ and $U_{\text{max}} \sim P_{\text{1D}}^{0.72}$, respectively, in excellent agreement with the experimental data. The blue diamonds correspond to 2D model calculations for a completely wetting liquid with $\Pi = 0$ and the first criterion using $h_{\text{crit}} = 5h^* = 50$ nm. The data are well represented by a power law $U_{\text{max}} \sim P^{1.1}$ and also agree well with the experimental data. We attribute the small differences relative to the 1D model calculations primarily due to

differences in the temperature distributions. Because of prohibitive computational cost, we could not include the disjoining pressure in our 2D calculations or use a contact angle larger than 10° in our 1D calculations. Overall, the agreement is remarkable, given that the disjoining pressure parameters are determined with a highest sensitivity to a film thickness range [74] of 40–400 nm.

V. SUMMARY AND CONCLUSIONS

We study the deformation and destabilization of thin liquid films on polymeric substrates by means of infrared laser illumination. The substrates are moving with respect to the laser beam. The intensity distribution of the laser beam is measured with a home-built scanning slit setup. In the case of wetting substrates, we measure the thickness profile of the deformed film by using dual-wavelength interference microscopy. We develop numerical models for the temperature distribution of the substrate and the subsequent redistribution of the liquid film based on the lubrication approximation.

In the case of a moving substrate, the driving force of the liquid redistribution (i.e., the in-plane temperature gradients at the liquid-air interface) strongly depends on the speed of the substrate and is determined by either conduction or convection of heat. The experimental and numerical results for the film thickness profile as a function of laser power and substrate speed are in good agreement, provided the temperature dependence of viscosity is properly accounted for.

In the case of a partially wetting substrate, the thin films can become unstable and rupture when sufficiently thinned. We find that it is possible to nucleate only a *single* dry spot for certain ranges of the substrate speed and laser power. The local temperature rise reduces the viscosity, which enhances the contact line mobility and thus the expansion rate of the dry spot; i.e., the liquid is displaced in a shorter time than would be necessary for the nucleation of a second dry spot. The thin film then dewets the substrate without leaving any residual droplets behind, which are commonly observed with other destabilization techniques [75]. Residue-free dewetting is desirable for several technological applications such as immersion lithography and solution processing of organic electronic devices.

ACKNOWLEDGMENTS

This work is part of the research program ‘‘Contact Line Control during Wetting and Dewetting’’ (CLC) of the ‘‘Stichting voor Fundamenteel Onderzoek der Materie (FOM),’’ which is financially supported by the ‘‘Nederlandse Organisatie voor Wetenschappelijk Onderzoek (NWO).’’ The CLC program is cofinanced by ASML and Oc . Moreover, the authors gratefully acknowledge that this research is supported partially by the Dutch Technology Foundation STW, applied science division of

NWO, and the Technology Program of the Ministry of Economic Affairs.

APPENDIX A: HEAT-TRANSFER MODEL

For a substrate that is moving in the y direction with a speed U_{sub} , the temperature distribution $T(x, y, z, t)$ is described by the heat-transfer equation [82]

$$\rho_{\text{sub}} c_p \left(\frac{\partial T}{\partial t} + U_{\text{sub}} \frac{\partial T}{\partial y} \right) = k_{\text{sub}} \nabla^2 T + \dot{q}. \quad (\text{A1})$$

The second term on the left-hand side of Eq. (A1) represents the convection of heat by the motion of the substrate. The term $\dot{q} \equiv \alpha_{\text{PC}} I$ represents a heat source as a consequence of laser light absorption [83–85], where $I(x, y, z)$ is the intensity distribution of the laser light [given by Eq. (1)].

Figure 12(a) shows a sketch of the three-dimensional computational domain of the thermal model with dimensions of $x_d = 2$ mm, $y_{d1} = -1$ mm, and $y_{d2} = 3$ mm. We use the following boundary conditions:

$$\frac{\partial T}{\partial x}(x=0) = \frac{\partial T}{\partial x}(x=x_d) = 0, \quad (\text{A2})$$

$$\frac{\partial T}{\partial y}(y=y_{d1}) = \frac{\partial T}{\partial y}(y=y_{d2}) = 0, \quad (\text{A3})$$

$$-k_{\text{sub}} \frac{\partial T}{\partial z}(z=0) = k_{\text{sub}} \frac{\partial T}{\partial z}(z=-d_{\text{sub}}) = \phi_{\text{loss}}. \quad (\text{A4})$$

The first part of Eq. (A2) reflects the mirror symmetry of the problem with respect to the plane $x=0$. The value of x_d is chosen sufficiently large so that the temperature rise does not reach the right boundary. At $y=y_{d1}$ and $y=y_{d2}$ we employ the so-called convective boundary condition; i.e., we assume that the diffusive fluxes $k_{\text{sub}}(\partial T/\partial y)(y=y_{d1})$ and $-k_{\text{sub}}(\partial T/\partial y)(y=y_{d2})$ are negligible compared to the convective fluxes $\rho_{\text{sub}} c_p U_{\text{sub}} T_0$ and $\rho_{\text{sub}} c_p U_{\text{sub}} T(y=y_{d2})$.

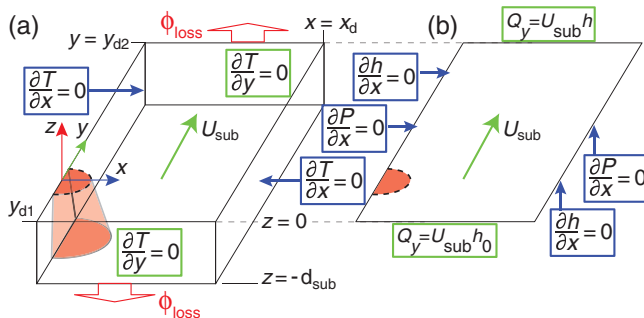


FIG. 12. Schematic representation of the computational domains and the applied boundary conditions of (a) the three-dimensional heat-transfer model and (b) the two-dimensional thin-film model.

We approximate the heat loss on the top and bottom surfaces of the substrate ($z=0$ and $z=-d_{\text{sub}}$, respectively) as a superposition of Newtonian convective cooling and thermal radiation:

$$\phi_{\text{loss}} = h_N(T - T_\infty) + \epsilon \sigma_B(T^4 - T_\infty^4). \quad (\text{A5})$$

Here, $\sigma_B = 5.67 \times 10^{-8}$ W/(m²K⁴) is the Stefan-Boltzmann constant, $\epsilon = 1$ is the thermal emissivity, $h_N = 5$ W/(m²K) the convective heat-transfer coefficient, and $T_\infty = T_0 = 293$ K the ambient temperature.

The presence of the liquid film is not accounted for in the thermal model, because its thickness on the order of $h_0 = 5$ μm is much smaller than $d_{\text{sub}} = 750$ μm, and its IR absorption, thus, is negligible.

All models are implemented by using the finite-element software COMSOL 3.5a.

1. Scaling analysis

For large U_{sub} , the two dominant terms in Eq. (A1) are

$$\rho_{\text{sub}} c_p U_{\text{sub}} \frac{\partial T}{\partial y} \sim \dot{q}, \quad (\text{A6})$$

where the relevant length scale in the heat source term \dot{q} is w_0 . The balance of these terms immediately yields the scaling relations $\max[\Delta T_s] \sim U_{\text{sub}}^{-1} \sim \text{Pe}_w^{-1}$ and $\max[\partial T_s/\partial y] \sim U_{\text{sub}}^{-1} \sim \text{Pe}_w^{-1}$, which are consistent with the results of Figs. 4(b) and 4(d).

The asymptotic behavior of the center line temperature in the limit of large distances from the laser spot is governed by the Green's function solution for an instantaneous plane source [82] with strength $\sim U_{\text{sub}}^{-1}$ upon replacing the time variable with y/U_{sub} :

$$\Delta T_s(y \gg 2w_0) \sim \frac{1}{\sqrt{4\pi\kappa U_{\text{sub}} y}} \exp\left(-\frac{U_{\text{sub}} x^2}{4\kappa y}\right), \quad (\text{A7})$$

where $\kappa \equiv k_{\text{sub}}/(\rho_{\text{sub}} c_p)$ is the thermal diffusivity of the substrate. In this limit, temperature gradients in the y and z directions become negligible compared to gradients in the x direction. The predicted asymptotic behavior for the centerline temperature is thus $\Delta T_s(x=0, y \gg w_0) \sim (\kappa U_{\text{sub}} y)^{-1/2}$. The relation $\Delta T_s \sim y^{-1/2}$ is indeed found in Fig. 4(a), and the relation $\Delta T_s \sim U_{\text{sub}}^{-1/2}$ is also verified (data not shown).

According to Eq. (A7), the asymptotic behavior for the FWHM of the temperature profile is $\text{FWHM} \sim \sqrt{\kappa y/U_{\text{sub}}}$. The relation $\text{FWHM} \sim y^{1/2}$ is reproduced in Fig. 3(a), and the relation $\text{FWHM} \sim U_{\text{sub}}^{-1/2}$ is also verified (data not shown).

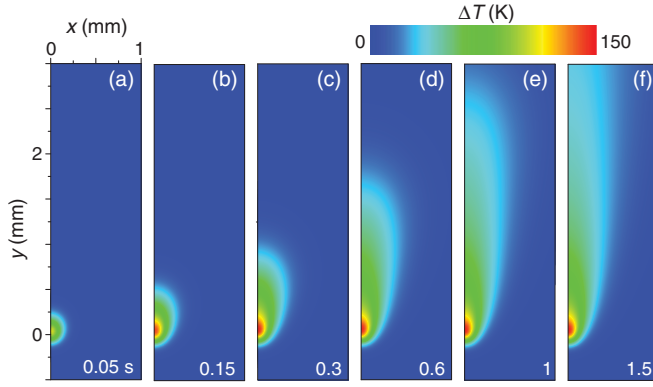


FIG. 13. Simulations of the surface temperature profile $\Delta T_s(x, y, t)$ at different times t for $P = 8$ W and $U_{\text{sub}} = 3$ mm/s.

APPENDIX B: TIME-DEPENDENT TEMPERATURE DISTRIBUTION

Figure 13 shows simulations of the surface temperature profile $\Delta T_s(x, y, t) \equiv T(x, y, z = 0, t) - T_0$ at different times t for a laser power $P = 8$ W and the substrate speed $U_{\text{sub}} = 3$ mm/s. The laser is switched on at $t = 0$. The position of maximum temperature rise is not located at the position of maximum intensity ($x = 0, y = 0$) but at a slightly larger value of y .

Figure 14(a) shows the surface temperature rise $\Delta T_s(x = 0, y, t)$ along the track center line ($x = 0$) of the profile. All parameters are the same as for Fig. 13. It shows that the maximum temperature rise is reached already after approximately 0.1 s. Convection of heat in the y direction causes the temperature profile to elongate. The thicker, orange line shows the steady-state temperature profile $\Delta T_s(t \rightarrow \infty)$. Figure 14(c) shows the y derivative of the temperature along the center line, $(\partial T_s / \partial y)(x = 0, y, t)$. Its maximum value $\max[\partial T_s / \partial y]$, indicated in Fig. 14(c) with the label “max,” increases in time and rapidly reaches a steady value. The minimum absolute value of this derivative, $|\min[\partial T_s / \partial y]|$, labeled “min” in Fig. 14(c), first increases and then decreases in time. The thicker, orange line shows the steady-state surface temperature gradient $(\partial T_s / \partial y)(t \rightarrow \infty)$. Because of the motion-induced asymmetry of the temperature profile, the maximum value of the steady-state temperature gradient is larger than its minimum absolute value.

In Ref. [70], we show that, in the case of a stationary substrate, the time scales for reaching a steady-state temperature or a steady-state temperature gradient are very different (as is explained in Supplemental Material [76]). In the case of a moving substrate and for the values of Pe_w considered in this study, these time scales are quite comparable.

Figures 14(b) and 14(d) show the steady-state values of $\max[\Delta T_s]$, $\max[\partial T_s / \partial y]$ and $|\min[\partial T_s / \partial y]|$, as a function

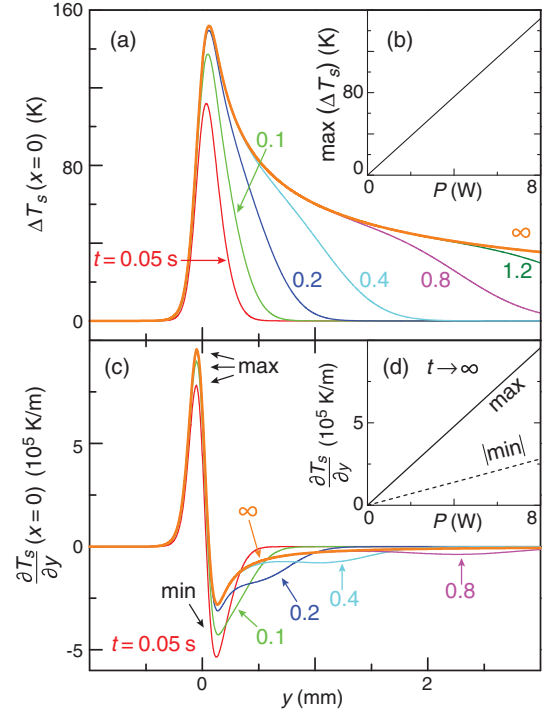


FIG. 14. Numerical results from the heat-transfer model. (a) Surface temperature rise along the track center line, $\Delta T_s(x = 0, y, t)$. (b) Maximum temperature rise in steady-state $\max[\Delta T_s(t \rightarrow \infty)]$ as a function of P . (c) Surface temperature gradient along the track center line $\partial T_s / \partial y(x = 0, y, t)$. (d) Maximum and minimum absolute values of the temperature gradient in the steady state, $\max[(\partial T_s / \partial y)(t \rightarrow \infty)]$ and $|\min[(\partial T_s / \partial y)(t \rightarrow \infty)]|$ as a function of P .

of the laser power P . Since the nonlinear radiative heat losses are small, all quantities scale linearly with P .

APPENDIX C: LUBRICATION MODEL

The lubrication equation [78] in Cartesian coordinates is given by

$$\frac{\partial h}{\partial t} + \frac{\partial Q_x}{\partial x} + \frac{\partial Q_y}{\partial y} = 0, \quad (\text{C1})$$

where the fluxes Q_x and Q_y are defined, respectively, as

$$Q_x \equiv \frac{h^2}{2\mu(T)} \tau_x - \frac{h^3}{3\mu(T)} \frac{\partial P}{\partial x}, \quad (\text{C2})$$

$$Q_y \equiv \frac{h^2}{2\mu(T)} \tau_y - \frac{h^3}{3\mu(T)} \frac{\partial P}{\partial y} + U_{\text{sub}} h. \quad (\text{C3})$$

The augmented pressure

$$P \equiv -\gamma(T) \left(\frac{\partial^2 h}{\partial x^2} + \frac{\partial^2 h}{\partial y^2} \right) + \rho(T) g h - \Pi(h) \quad (\text{C4})$$

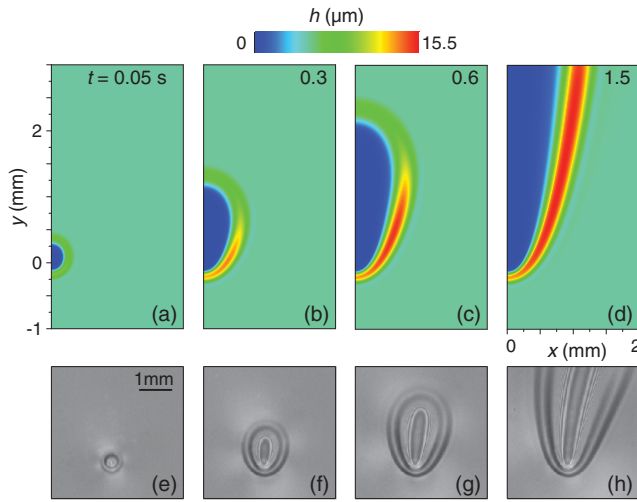


FIG. 15. (a)–(d) Simulations of the thin-liquid-film profile $h(x, y, t)$ at different times for $P = 8$ W and $U_{\text{sub}} = 3$ mm/s. (e)–(h) Corresponding experimental interference micrographs for $P = 8$ W and $U_{\text{sub}} = 3.1$ mm/s.

represents the influence of capillary pressure, hydrostatic pressure, and the disjoining pressure Π [86]. The values of surface tension $\gamma(T)$, viscosity $\mu(T)$, and density $\rho(T)$ are given in Supplemental Material [76]. For the simulation of partially wetting liquids we use Eq. (6) for the disjoining pressure, and for completely wetting liquids we set $\Pi = 0$.

The terms τ_x and τ_y

$$\tau_x \equiv \frac{\partial \gamma}{\partial x} = \frac{\partial \gamma}{\partial T} \frac{\partial T_l}{\partial x} \quad \text{and} \quad \tau_y \equiv \frac{\partial \gamma}{\partial y} = \frac{\partial \gamma}{\partial T} \frac{\partial T_l}{\partial y} \quad (\text{C5})$$

are the thermocapillary shear stresses that act on the thin film. Here, T_l is the temperature at the liquid-air interface, which is essentially equal to the surface temperature of the substrate $T_l = T(x, y, z = 0, t)$, since the thickness of the liquid film is small, $h_0 \ll d_{\text{sub}}$. We extract the substrate temperature from the heat-transfer calculations.

Figure 12(b) shows a sketch of the computational domain that we use for the thin-film model. We use the following boundary conditions:

$$\frac{\partial h}{\partial x}(x = 0) = 0, \quad \frac{\partial \mathcal{P}}{\partial x}(x = 0) = 0, \quad (\text{C6})$$

$$\frac{\partial h}{\partial x}(x = x_d) = 0, \quad \frac{\partial \mathcal{P}}{\partial x}(x = x_d) = 0, \quad (\text{C7})$$

$$h(y = y_{d1}) = h_0, \quad Q_y(y = y_{d1}) = U_{\text{sub}} h_0, \quad (\text{C8})$$

$$\frac{\partial h}{\partial y}(y = y_{d2}) = 0, \quad Q_y(y = y_{d2}) = U_{\text{sub}} h. \quad (\text{C9})$$

Equation (C6) reflects the mirror symmetry of the problem with respect to the track center line. The domain width

$x = x_d$ is chosen sufficiently large so that the thin-film deformation does not reach the lateral boundary of the domain. Equations (C8) and (C9) reflect the motion of the substrate: The thin film enters the domain with a volume flux $Q_y = U_{\text{sub}} h_0$ at $y = y_{d1}$ and leaves the domain with volume flux $Q_y = U_{\text{sub}} h$ at $y = y_{d2}$. The initial condition is a film of uniform thickness $h(x, y, t = 0) = h_0$.

APPENDIX D: TIME-DEPENDENT THIN-FILM DEFORMATION

Figure 15 illustrates the deformation of a thin squalane film on a PC substrate for $U_{\text{sub}} = 3$ mm/s and a laser power of $P = 8$ W. Figures 15(a)–15(d) are obtained from a numerical simulation and Figs. 15(e)–15(h) from an experiment. The interference micrographs show the film deformation at approximately the same times t as the corresponding images in Figs. 15(a)–15(d). Figures 15(d)–15(h) essentially correspond to the steady-state height profiles.

- [1] L. Wu, Modelling and simulation of the lubricant depletion process induced by laser heating in heat-assisted magnetic recording system, *Nanotechnology* **18**, 215702 (2007).
- [2] N. Tagawa, R. Kakitani, H. Tani, N. Iketani, and I. Nakano, Study of lubricant depletion induced by laser heating in thermally assisted magnetic recording systems-effect of lubricant film materials, *IEEE Trans. Magn.* **45**, 877 (2009).
- [3] H. E. Cline and T. R. Anthony, Heat treating and melting material with a scanning laser or electron-beam, *J. Appl. Phys.* **48**, 3895 (1977).
- [4] H. E. Cline, Surface rippling induced in thin-films by a scanning laser, *J. Appl. Phys.* **52**, 443 (1981).
- [5] Y. Nabetani, H. Yoshikawa, A. C. Grimsdale, K. Müellen, and H. Masuhara, Effects of optical trapping and liquid surface deformation on the laser microdeposition of a polymer assembly in solution, *Langmuir* **23**, 6725 (2007).
- [6] N. R. Bieri, J. Chung, D. Poulikakos, and C. P. Grigoropoulos, An experimental investigation of micro-resistor laser printing with gold nanoparticle-laden inks, *Appl. Phys. A* **80**, 1485 (2005).
- [7] J. B. Brzoska, F. Brochard-Wyart, and F. Rondelez, Motions of droplets on hydrophobic model surfaces induced by thermal gradients, *Langmuir* **9**, 2220 (1993).
- [8] M. K. Smith, Thermocapillary migration of a two-dimensional liquid droplet on a solid surface, *J. Fluid Mech.* **294**, 209 (1995).
- [9] B. A. Bezuglyi and N. A. Ivanova, Gas bubbles in a Hele-Shaw cell manipulated by a light beam, *Tech. Phys. Lett.* **28**, 828 (2002).
- [10] A. A. Darhuber, J. P. Valentino, S. M. Troian, and S. Wagner, Thermocapillary actuation of droplets on chemically patterned surfaces by programmable microheater arrays, *J. Microelectromech. Syst.* **12**, 873 (2003).
- [11] A. A. Darhuber, J. M. Davis, S. M. Troian, and W. W. Reisner, Thermocapillary actuation of liquid flow on

- chemically patterned surfaces, *Phys. Fluids* **15**, 1295 (2003).
- [12] S. Rybalko, N. Magome, and K. Yoshikawa, Forward and backward laser-guided motion of an oil droplet, *Phys. Rev. E* **70**, 046301 (2004).
- [13] A. A. Darhuber and S. M. Troian, Principles of microfluidic actuation by modulation of surface stresses, *Annu. Rev. Fluid Mech.* **37**, 425 (2005).
- [14] K. T. Kotz, Y. Gu, and G. W. Faris, Optically addressed droplet-based protein assay, *J. Am. Chem. Soc.* **127**, 5736 (2005).
- [15] T. H. Ting, Y. F. Yap, N.-T. Nguyen, T. N. Wong, J. C. K. Chai, and L. Yobas, Thermally mediated breakup of drops in microchannels, *Appl. Phys. Lett.* **89**, 234101 (2006).
- [16] C. N. Baroud, M. R. de Saint Vincent, and J.-P. Delville, An optical toolbox for total control of droplet microfluidics, *Lab Chip* **7**, 1029 (2007).
- [17] A. S. Basu and Y. B. Gianchandani, Virtual microfluidic traps, filters, channels and pumps using Marangoni flows, *J. Micromech. Microeng.* **18**, 115031 (2008).
- [18] Z. Jiao, X. Huang, N.-T. Nguyen, and P. Abgrall, Thermocapillary actuation of droplet in a planar microchannel, *Microfluid. Nanofluid.* **5**, 205 (2008).
- [19] M. R. de Saint Vincent, R. Wunenburger, and J.-P. Delville, Laser switching and sorting for high speed digital microfluidics, *Appl. Phys. Lett.* **92**, 154105 (2008).
- [20] J.-P. Delville, M. R. de Saint Vincent, R. D. Schroll, H. Chraïbi, B. Isenmann, R. Wunenburger, D. Lasseux, W. W. Zhang, and E. Brasselet, Laser microfluidics: Fluid actuation by light, *J. Opt. A* **11**, 034015 (2009).
- [21] R. Shukla and K. A. Sallam, Effect of liquid transparency on laser-induced motion of drops, *J. Fluid Eng.* **131**, 081301 (2009).
- [22] B. Selva, I. Cantat, and M.-C. Jullien, Temperature-induced migration of a bubble in a soft microcavity, *Phys. Fluids* **23**, 052002 (2011).
- [23] W. Hu and A. T. Ohta, Aqueous droplet manipulation by optically induced Marangoni circulation, *Microfluid. Nanofluid.* **11**, 307 (2011).
- [24] M. R. de Saint Vincent and J.-P. Delville, Thermocapillary migration in small-scale temperature gradients: Application to optofluidic drop dispensing, *Phys. Rev. E* **85**, 026310 (2012).
- [25] E. Heintz, Deux procédés nouveaux de photographie infrarouge. II, *J. Phys. Radium* **7**, 336 (1946).
- [26] M. Cormier, M. Blanchard, M. Rioux, and R. Beaulieu, Holographie en infrarouge sur de minces couches d'huile, *Appl. Opt.* **17**, 3622 (1978).
- [27] J. C. Loulergue, Y. Levy, and C. Imbert, Thermal imaging system with a two-phase ternary mixture of liquids, *Opt. Commun.* **45**, 149 (1983).
- [28] V. Ludviksson and E. N. Lightfoot, The dynamics of thin liquid films in the presence of surface-tension gradients, *AIChE J.* **17**, 1166 (1971).
- [29] A. M. Cazabat, F. Heslot, S. M. Troian, and P. Carles, Fingering instability of thin spreading films driven by temperature gradients, *Nature (London)* **346**, 824 (1990).
- [30] D. E. Kataoka and S. M. Troian, Stabilizing the advancing front of thermally driven climbing films, *J. Colloid Interface Sci.* **203**, 335 (1998).
- [31] J. Bischof, D. Scherer, S. Herminghaus, and P. Leiderer, Dewetting Modes of Thin Metallic Films: Nucleation of Holes and Spinodal Dewetting, *Phys. Rev. Lett.* **77**, 1536 (1996).
- [32] D. A. Willis and X. Xu, Transport phenomena and droplet formation during pulsed laser interaction with thin films, *J. Heat Transfer* **122**, 763 (2000).
- [33] V. S. Ajaev and D. A. Willis, Thermocapillary flow and rupture in films of molten metal on a substrate, *Phys. Fluids* **15**, 3144 (2003).
- [34] C. Favazza, R. Kalyanaraman, and R. Sureshkumar, Dynamics of ultrathin metal films on amorphous substrates under fast thermal processing, *J. Appl. Phys.* **102**, 104308 (2007).
- [35] J. Trice, D. Thomas, C. Favazza, R. Sureshkumar, and R. Kalyanaraman, Pulsed-laser-induced dewetting in nanoscopic metal films: Theory and experiments, *Phys. Rev. B* **75**, 235439 (2007).
- [36] A. Atena and M. Khenner, Thermocapillary effects in driven dewetting and self assembly of pulsed-laser-irradiated metallic films, *Phys. Rev. B* **80**, 075402 (2009).
- [37] A. Dun, J. Wei, and F. Gan, Marangoni effect induced micro/nano-patterning on Sb₂Te₃ phase change thin film by laser pulse, *Appl. Phys. A* **103**, 139 (2011).
- [38] J. A. Vieyra Salas, J. M. van der Veen, J. J. Michels, and A. A. Darhuber, Active control of evaporative solution deposition by modulated infrared illumination, *J. Phys. Chem. C* **116**, 12038 (2012).
- [39] A. V. Hershey, Ridges in a liquid surface due to the temperature dependence of surface tension, *Phys. Rev.* **56**, 204 (1939).
- [40] G. Da Costa and J. Calatroni, Self-holograms of laser-induced surface depressions in heavy hydrocarbons, *Appl. Opt.* **17**, 2381 (1978).
- [41] G. Da Costa and J. Calatroni, Transient deformation of liquid surfaces by laser-induced thermocapillarity, *Appl. Opt.* **18**, 233 (1979).
- [42] S. M. Pimputkar and S. Ostrach, Transient thermocapillary flow in thin liquid layers, *Phys. Fluids* **23**, 1281 (1980).
- [43] H. Helmers and W. Witte, Holographic study of laser-induced liquid surface deformations, *Opt. Commun.* **49**, 21 (1984).
- [44] J. P. Burelbach, S. G. Bankoff, and S. H. Davis, Steady thermocapillary flows of thin liquid layers. II. Experiment, *Phys. Fluids A* **2**, 322 (1990).
- [45] M. J. Tan, S. G. Bankoff, and S. H. Davis, Steady thermocapillary flows of thin liquid layers. I. Theory, *Phys. Fluids A* **2**, 313 (1990).
- [46] D. Schwabe, U. Möller, J. Schneider, and A. Scharmann, Instabilities of shallow dynamic thermocapillary liquid layers, *Phys. Fluids A* **4**, 2368 (1992).
- [47] D. L. Hitt and M. K. Smith, Radiation-driven thermocapillary flows in optically thick liquid films, *Phys. Fluids A* **5**, 2624 (1993).
- [48] J. P. Longtin, K. Hijikata, and K. Ogawa, Laser-induced surface-tension-driven flows in liquids, *Int. J. Heat Mass Transfer* **42**, 85 (1999).
- [49] B. A. Bezuglyi and A. A. Fedorets, Measuring the thickness of thin liquid films on solid surfaces using the laser-induced thermocapillary response, *Tech. Phys. Lett.* **27**, 359 (2001).

- [50] R. O. Grigoriev, Control of evaporatively driven instabilities of thin liquid films, *Phys. Fluids* **14**, 1895 (2002).
- [51] M. Bestehorn, A. Pototsky, and U. Thiele, 3D large scale Marangoni convection in liquid films, *Eur. Phys. J. B* **33**, 457 (2003).
- [52] A. I. Mizev, Experimental investigation of thermocapillary convection induced by a local temperature inhomogeneity near the liquid surface. 2. Radiation-induced source of heat, *J. Appl. Mech. Tech. Phys.* **45**, 699 (2004).
- [53] S. P. Karlov, D. A. Kazenin, B. I. Myznikova, and I. I. Wertgeim, Experimental and numerical study of the Marangoni convection due to localized laser heating, *J. Non-Equilib. Thermodyn.* **30**, 283 (2005).
- [54] S. Saprykin, P. M. J. Trevelyan, R. J. Koopmans, and S. Kalliadasis, Free-surface thin-film flows over uniformly heated topography, *Phys. Rev. E* **75**, 026306 (2007).
- [55] I. V. Marchuk, Thermocapillary deformation of a thin locally heated horizontal liquid layer, *J. Eng. Thermophys.* **18**, 227 (2009).
- [56] H. Chraïbi and J.-P. Delville, Thermocapillary flows and interface deformations produced by localized laser heating in confined environment, *Phys. Fluids* **24**, 032102 (2012).
- [57] B. S. Tilley and M. Bowen, Thermocapillary control of rupture in thin viscous fluid sheets, *J. Fluid Mech.* **541**, 399 (2005).
- [58] M. Bowen and B. S. Tilley, Thermally induced van der Waals rupture of thin viscous fluid sheets, *Phys. Fluids* **24**, 032106 (2012).
- [59] V. V. Pukhnachev and S. B. Dubinkina, A model of film deformation and rupture under the action of thermocapillary forces, *Fluid Dyn.* **41**, 755 (2006).
- [60] A. S. Ovcharova, Features of the rupture of free hanging liquid film under the action of a thermal load, *Phys. Fluids* **23**, 102106 (2011).
- [61] A. S. Ovcharova, Effect of the thermophysical properties of the liquid on the rupture of a film under a thermal load. Role of the Prandtl number, *J. Appl. Mech. Tech. Phys.* **53**, 182 (2012).
- [62] A. Sharon and A. Orell, Dry patch formation in liquid films flowing in a heated horizontal channel, *Int. J. Heat Mass Transfer* **23**, 547 (1980).
- [63] E. Hasegawa and J. Kojima, Breakup of a thin liquid layer heated from below, *Bull. JSME* **26**, 380 (1983).
- [64] A. L. Zuev and A. F. Pshenichnikov, Deformation and breakup of a liquid film under the action of thermocapillary convection, *J. Appl. Mech. Tech. Phys.* **28**, 399 (1987).
- [65] B. A. Bezuglyi and O. A. Tarasov, Effect of the ellipticity of an inducing beam on the thermocapillary response, *Opt. Spectrosc.* **94**, 230 (2003).
- [66] Y. O. Kabova, A. Alexeev, T. Gambaryan-Roisman, and P. Stephan, Marangoni-induced deformation and rupture of a liquid film on a heated microstructured wall, *Phys. Fluids* **18**, 012104 (2006).
- [67] D. V. Zaitsev, D. A. Rodionov, and O. A. Kabov, Study of thermocapillary film rupture using a fiber optical thickness probe, *Microgravity Sci. Technol.* **19**, 100 (2007).
- [68] S. Krishnamoorthy, B. Ramaswamy, and S. W. Joo, Spontaneous rupture of thin liquid films due to thermocapillarity: A full-scale direct numerical simulation, *Phys. Fluids* **7**, 2291 (1995).
- [69] A. Oron and S. G. Bankoff, Dewetting of a heated surface by an evaporating liquid film under conjoining/disjoining pressures, *J. Colloid Interface Sci.* **218**, 152 (1999).
- [70] H. M. J. M. Wedershoven, C. W. J. Berendsen, J. C. H. Zeegers, and A. A. Darhuber, Infrared laser induced rupture of thin liquid films on stationary substrates, *Appl. Phys. Lett.* **104**, 054101 (2014).
- [71] J. P. Singer, P.-T. Lin, S. E. Kooi, L. C. Kimerling, J. Michel, and E. L. Thomas, Direct-write thermocapillary dewetting of polymer thin films by a laser-induced thermal gradient, *Adv. Mater.* **25**, 6100 (2013).
- [72] M. Switkes and M. Rothschild, Immersion lithography at 157 nm, *J. Vac. Sci. Technol. B* **19**, 2353 (2001).
- [73] R. H. French and H. V. Tran, Immersion lithography: Photomask and wafer-level materials, *Annu. Rev. Mater. Res.* **39**, 93 (2009).
- [74] C. W. J. Berendsen, J. C. H. Zeegers, G. C. F. L. Kruis, M. Riepen, and A. A. Darhuber, Rupture of thin liquid films induced by impinging air-jets, *Langmuir* **28**, 9977 (2012).
- [75] C. W. J. Berendsen, J. C. H. Zeegers, and A. A. Darhuber, Deformation and dewetting of thin liquid films induced by moving gas jets, *J. Colloid Interface Sci.* **407**, 505 (2013).
- [76] See Supplemental Material <http://link.aps.org/supplemental/10.1103/PhysRevApplied.3.024005> at for a movie of infrared-laser-induced dewetting on a moving substrate, information on material properties, an experimental verification of the heat-transfer model, information on the effect of vertical substrate misalignment, and information on the effect of the substrate thickness on the heat transfer.
- [77] R. L. McCally, Measurement of Gaussian beam parameters, *Appl. Opt.* **23**, 2227 (1984).
- [78] A. Oron, S. H. Davis, and S. G. Bankoff, Long-scale evolution of thin liquid films, *Rev. Mod. Phys.* **69**, 931 (1997).
- [79] D. J. Sanders, Temperature distributions produced by scanning Gaussian laser beams, *Appl. Opt.* **23**, 30 (1984).
- [80] L. W. Schwartz and R. R. Eley, Simulation of droplet motion on low-energy and heterogeneous surfaces, *J. Colloid Interface Sci.* **202**, 173 (1998).
- [81] B. J. Brasjen and A. A. Darhuber, Dry-spot nucleation in thin liquid films on chemically patterned surfaces, *Microfluid. Nanofluid.* **11**, 703 (2011).
- [82] H. S. Carslaw and J. C. Jaeger, *Conduction of Heat in Solids* (Oxford University Press, New York, 1959).
- [83] M. L. Cordero, E. Verneuil, F. Gallaire, and C. N. Baroud, Time-resolved temperature rise in a thin liquid film due to laser absorption, *Phys. Rev. E* **79**, 011201 (2009).
- [84] H. J. Eichler, P. Günter, and D. W. Pohl, *Laser-Induced Dynamic Gratings* (Springer-Verlag, Berlin, 1986).
- [85] P. Schaaf, *Laser Processing of Materials* (Springer-Verlag, Berlin, 2010).
- [86] B. V. Deryagin, The definition and magnitude of disjoining pressure and its role in the statics and dynamics of thin fluid films, *Kolloid Zh.* **17**, 205 (1955).